

HELIOSEISMOLOGY OF PRE-EMERGING ACTIVE REGIONS. I. OVERVIEW, DATA, AND TARGET SELECTION CRITERIA

K. D. LEKA¹, G. BARNES¹, A. C. BIRCH^{1,3}, I. GONZALEZ-HERNANDEZ², T. DUNN¹, B. JAVORNIK¹, AND D. C. BRAUN¹

¹ NorthWest Research Associates, Boulder, CO 80301, USA

² National Solar Observatory, Tucson, AZ 85719, USA

³ Max-Planck Institut für Sonnensystemforschung, D-37191 Kalenburg-Lindau, Germany

Received 2012 August 9; accepted 2012 November 13; published 2012 December 21

ABSTRACT

This first paper in a series describes the design of a study testing whether pre-appearance signatures of solar magnetic active regions were detectable using various tools of local helioseismology. The ultimate goal is to understand flux-emergence mechanisms by setting observational constraints on pre-appearance subsurface changes, for comparison with results from simulation efforts. This first paper provides details of the data selection and preparation of the samples, each containing over 100 members, of two populations: regions on the Sun that produced a numbered NOAA active region, and a “control” sample of areas that did not. The seismology is performed on data from the GONG network; accompanying magnetic data from *SOHO*/MDI are used for co-temporal analysis of the surface magnetic field. Samples are drawn from 2001–2007, and each target is analyzed for 27.7 hr prior to an objectively determined time of emergence. The results of two analysis approaches are published separately: one based on averages of the seismology- and magnetic-derived signals over the samples, another based on Discriminant Analysis of these signals, for a statistical test of detectable differences between the two populations. We include here descriptions of a new potential-field calculation approach and the algorithm for matching sample distributions over multiple variables. We describe known sources of bias and the approaches used to mitigate them. We also describe unexpected bias sources uncovered during the course of the study and include a discussion of refinements that should be included in future work on this topic.

Key words: methods: data analysis – Sun: helioseismology – Sun: interior – Sun: oscillations – Sun: surface magnetism – Sunspots

1. INTRODUCTION

We refer to the appearance of new solar active regions as “emergence,” implying a rise from below the visible photosphere. Yet the appearance and evolution of an active region from the surface through the corona is the symptom, the result—filtered through the $\tau = 1$ boundary and the transitions from high- to low- β plasmas—of some (yet unknown) process happening below the visible surface.

One general class of theories suggests that active regions form as the result of magnetic flux concentrations rising buoyantly from the base of the convection zone (for a review see Fan 2009). Another possibility is that sunspots are formed via coagulation of magnetic fields generated closer to the solar surface (Brandenburg 2005 and references therein). The pre-emergence (PE) seismic signatures expected from these two approaches differ substantially. From the former scenario, one should expect signals generally taking the form of a bulk and quickly moving disturbance whose internal plasma flow should result in a signal detectable with today’s tools (Birch et al. 2010). In the latter case, the expectation would likely be a slower change in the subsurface temperature, flow, and magnetic field environment over a less localized area. Simulations which focus on the dynamics of flux systems rising through the upper layers imply that slowly rising flux systems may impact the convection only minimally (Stein et al. 2011), depending on the field strengths involved. Still, simulations provide clues but are limited; observations must continue to provide guidance.

Being able to peer below the visible surface at the subsurface structure and dynamics could provide the guidance regarding the formation mechanism for solar active regions (“AR”). Helioseismology seems to promise the ability to detect changes in the

flow patterns and temperature beneath the visible surface. From the pure physics perspective, the tools of local helioseismology (Gizon & Birch 2005; Gizon et al. 2010) should help determine the subsurface dynamics associated with active-region formation, and thus could provide evidence for or against the basic model types. Some preliminary work (described below) applying sensitive tools of this type to data sets well suited for these techniques suggests that the capability may now be available.

Most recent efforts have been case studies, focusing on the emergence of one or a few active regions (e.g., Jensen et al. 2001; Zharkov & Thompson 2008; Komm et al. 2008; Ilonidis et al. 2011; Braun 2012). The results have been inconclusive when taken as an ensemble, possibly due to the physics of active-region emergence, possibly due to the differences between the studies themselves. Inverting time-distance data from the Michelson Doppler Imager (MDI) using three-dimensional kernels, Jensen et al. (2001) found perturbations indicating wave-speed increases 20 Mm below two active regions in the hours after their appearance. Zharkov & Thompson (2008), using a very similar method for two active regions, found a similar increase when surface flux was visible, but also a “loop-like structure” with decreased sound speed, days prior to the appearance of surface flux. Ilonidis et al. (2011) also employ time-distance analysis of MDI data, and present very large negative travel-time shifts (increases in the sound speed) located between 42 and 75 Mm up to two days prior to surface flux appearance of four active regions. They associate these disturbances with magnetic structures emerging at speeds of 0.3–0.6 km s⁻¹, and do see a high rate of flux emergence following the perturbations. Yet Braun (2012), using acoustic holography on the same data for the same four active regions, detect no such unique signals at the specified times and depths.

Employing ring-diagram analysis of GONG data for 13 new or growing active regions (and contrasting with control areas), Komm et al. (2008) found evidence for upflows prior to the appearance of emerging flux at the surface, followed by a transition to predominantly downflows once the active region was established.

Ring-diagram analysis was also used in statistical studies of seismic signatures associated with emerging magnetic flux, comparing average signals for hundreds of regions with increasing flux to either “quiet” areas or to those with decreasing flux (Komm et al. 2009, 2011). While the analysis had fairly low temporal and spatial resolution, upflows were associated with emerging flux at depths below 10 Mm whereas at shallower layers, upflows changed to downflows as surface field became stronger. These studies examined the broad spectrum of surface-field behavior: growing flux, consistent flux, and decreasing flux. However, the “emerging flux” category did not differentiate between “new” active regions and emerging flux within already established regions.

The conflicting results in case studies could indicate that there is no unique signature, or that results are sensitive to subtle methodology differences. The few published statistical studies have been based on a single method, and now need to be refined to focus solely on the pre-emergence context, and employ higher resolution analysis.

In the present investigation, we employ a combination of local helioseismology, surface magnetic field diagnostics, and statistical tests to examine what can be learned with regards to subsurface magnetic flux systems, their structure, and their evolution. The basic premise of this series of papers (this paper along with Birch et al. 2012; Barnes et al. 2012) is to determine if there are detectable changes in the solar interior that indicate an emerging active region prior to the appearance at the solar surface of a magnetic field concentration.

We have designed and completed a study to examine the possibility of pre-emergence detection of active regions, with the goal of characterizing the subsurface changes in the context of emerging-flux models. The approach pays attention to sources of bias, statistical and systematic error, and includes statistical validation of the results. The organization of this paper is as follows: In Section 2, we outline the physical parameters within which the overall study must work and the statistical motivation for the overall design of our study. We describe the data used and its treatment in Section 3, and in Section 3.1 describe the target selection criteria, justification, and implementation. We discuss sources of statistical contamination in Section 4. The most salient points are synthesized in Section 5 as groundwork for Birch et al. (2012), where the helioseismic analysis is presented, and for Barnes et al. (2012), where the statistical analysis of the helioseismic and magnetic data are presented.

2. STUDY DESIGN

The goal of this study is to determine whether there exists a pre-emergence signature of solar active regions visible using local helioseismic methods and understand said signal, if it exists, in the context of active-region formation theory. As summarized above, case studies have led to conflicting results. We have designed a study that utilizes appropriate statistical tests applied to data that include “control” samples. Such a study requires two basic things: sufficient samples of both “event” data and a control set, and care in selecting both samples so as to minimize bias.

It is fortunate now that there are sufficient data available to perform such a study, including a statistical analysis of the results. The statistical method we use in Barnes et al. (2012) is discriminant analysis (e.g., Kendall et al. 1983), a technique that tests for *any* difference between the two samples. As such, any systematic bias that is present in the sampling from one population but absent in the other may appear as a false discriminant. For example, if all samples for one population were obtained from east of central meridian while all samples for the other were obtained from west of central meridian, then the samples could be differentiated simply due to a bias in the Doppler signal from solar rotation, not a true detection of emergence. We refer to this bias as statistical contamination.

The basic data comprise time series of Doppler velocity obtained at the solar surface, from which shifts in subsurface travel times are derived using helioseismic holography (Lindsey & Braun 2000; Braun et al. 2007). Obtaining a reliable seismic signature requires a temporal sequence of data, the length of which will govern the signal-to-noise ratios of the inferred subsurface patterns; yet the data quality may degrade with proximity to the solar limb. These realities create limits on the observable solar disk available for drawing the samples.

In the case of analysis using helioseismology, bias may take many forms. Due to the global frequency shifts with solar cycle (Woodard & Noyes 1985; Christensen-Dalsgaard 2002; Chaplin et al. 2007), the Doppler velocity signals may have a component distinctly linked directly to the date. Systematic effects (Braun & Birch 2008; Zhao et al. 2012; Baldner & Schou 2012) may create a dependence of the helioseismology results on apparent disk position. Active regions emerge within a fairly narrow latitude range, which itself shifts with the phase of the activity cycle, leading to another potential source of bias.

To allow an unambiguous detection of subsurface signals, the emergence episodes should be isolated in time and space from other strong magnetic sources and nearby emergence episodes. Yet active regions often emerge in close proximity to already-established active regions or remnant fields (Petrovay & Abuzeid 1991; Harvey & Zwaan 1993; Pojoga & Cudnik 2002). The controls must ideally also have no magnetic emergence occurring, and minimal strong-field regions within the immediate field of view, but they must also match the magnetic context of the population of emerging targets, as the solar disk gets crowded with active regions and their remnants during the solar maximum years.

Thus, it is key to couple observations of the solar surface magnetic field and its evolution to the selection and characterization of the seismology data. Pairing the magnetic data to the seismic data provides guidance for interpreting any seismic signature observed, both in the control and event groups.

The study is designed based on the following steps.

1. Locate and identify a statistically significant sample of the population of new active region appearances, according to constraints imposed to minimize bias and noise.
2. Locate and identify a sample of the emergence-free population, matched in time and position to the pre-emergence sample, to serve as a control.
3. Apply helioseismic data analysis “blindly” to the two samples.
4. Parameterize the results from the helioseismic analysis and magnetic field data.
5. Apply Discriminant Analysis to the seismic and magnetic parameters to quantify the differences between the two samples.

3. DATA

A study such as this requires a statistically significant sample drawn from the populations in question. Limitations posed due to observational and statistical constraints, described in detail below, thus pointed to using data from the Global Oscillations Network Group (GONG), from the era after the camera upgrades (beginning in 2001, Harvey et al. 1998; Hill et al. 2003). The GONG system records wavelength-modulated full-disk images sampled at 2''.5 for 5'' optical resolution from which Doppler signals are retrieved on a 1 minute cadence.

Key to interpreting any detected seismic signature is knowing the “landscape” of the surface magnetic field. As we are specifically interested in pre-emergence signatures, the surface magnetic fields and the signature of magnetic flux emergence *define* the timing for the entire project. At the time of design and implementation of this study, the line-of-sight field from the GONG data was not readily available. We thus rely upon the full-disk line-of-sight component magnetic field data from the MDI aboard the *Solar and Heliospheric Observatory* (*SOHO*/MDI; Scherrer et al. 1995). Specifically, we used the level 1.8.2 synoptic data acquired with a 96 minute cadence and 1''.98 pixel size⁴ to qualitatively and quantitatively evaluate the magnetic landscape of the samples.

Helioseismic data from MDI were not used in this study for two reasons. First, the high-rate full-disk data (“dynamics campaigns”) are only available for a few months per year, limiting the data available for a statistical study. Second, the medium- ℓ (“structure”) data are not optimal for studying wave propagation at distances less than approximately ten heliocentric degrees (Giles 2000) whereas the present work examines depths $\lesssim 25$ Mm which requires small distances. For these reasons, we have used the GONG data for the helioseismic analysis performed in this study.

3.1. Target Selection Criteria: The “PEs”: Pre-emergence Regions

The initial target list for emerging active regions was derived from the “Sunspot Group Reports” produced by USAF/NOAA and available through the National Geophysical Data Center.⁵ The date range used was chosen according to requirements for the helioseismology data, and covered 2001 July–2007 November. Regions listed as first appearing within $\theta \leq 30^\circ$ of disk center and which achieved an area $> 10 \times 10^{-6}$ hemispheres (μH) during their disk passage determined the initial target list and the initial emergence times and locations that were subsequently refined.

MDI three-day time-series were constructed centered on this initial emergence date and time, using a fixed 128×100 pixel box centered on the initial emergence location (see Figure 1 for a schematic), and tracked with the synodic rotation rate (Figure 2). As a check against extreme viewing angles at the beginning or end of the time series, additional limits on the edges of the box were placed at E41 and W67 heliographic longitude (east longitudes are < 0) and $\pm 60^\circ$ heliographic latitude. The B_{los} data were initially summed to a pseudo-“flux,” $\Phi_{\text{los}} = \sum |B_{\text{los}}| / \mu \Delta A$, where $\mu = \cos \theta$ and θ is the observing angle, and ΔA is the physical area of a pixel. A refined emergence time, t_0 , was defined as the time of the first MDI

⁴ Emergence times were initially determined using earlier level 1.8.1 data, but we do not expect any systematic differences as the emergence times were based on the change of the signal, not a pre-determined threshold.

⁵ <http://www.ngdc.noaa.gov/stp/solar/sunspotregionsdata.html>

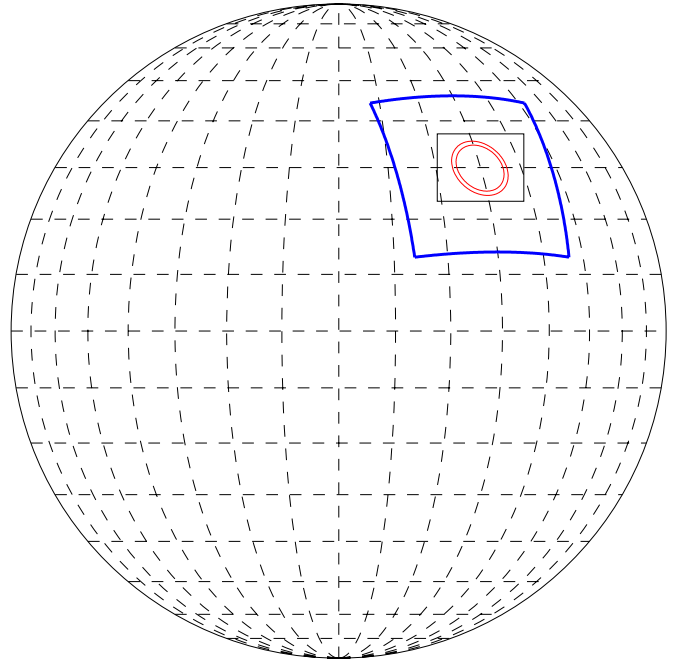


Figure 1. Schematic showing the relative sizes of areas considered during the data preparation and analysis. The solar Stonyhurst disk is shown with lines at 10° latitude and longitude intervals (---). The black box indicates the 128×100 pixel area of an MDI image used for the initial evaluation, in this case centered at N30 W30. The larger box (blue) is a Postel projection region $32^\circ \times 32^\circ$, showing the area extracted for the tracked Doppler data from GONG, and the corresponding area of computed radial component of the field from MDI extracted for the full analysis. The red circles indicate the size and width of the largest annulus (filter “TD11”) used for computing helioseismology parameters (see Birch et al. 2012).

observation after Φ_{los} reached 10% of the maximum achieved (minus any flux present at the beginning of the time series) over the time series. That is, the “10% rule” refers to 10% of the maximum increase detected. The kurtosis (fourth moment) of the distribution of B_{los} in the frame generally increases dramatically at the time of emergence, signifying a distinct change in the spatial distribution of B_{los} ; a sudden change in the kurtosis was used to confirm the “10% rule” but was not relied upon in isolation. Thus, the emergence time is only defined within the 96 minute MDI cadence. For the analysis methods later applied, which require many hours of data, there is little to be gained by refining this definition further. The NOAA reports of active region coordinates were generally accurate, although our definition of t_0 was generally earlier than the NOAA reports by anywhere from a few hours up to a day.

Emergence of surface field is rarely a smoothly monotonic process (Zwaan 1985; Leka et al. 1994; Kubo et al. 2003). An example of that reality is shown in Figure 3 (and discussed further in Section 4.3). As such, the flux history and thresholds here constitute a selection rule to be used for a statistical approach, rather than a profound statement of solar physics. And as such, there will be regions for which the definition blatantly misses the mark of rising flux presence. The goal here is a well-defined “good option,” which is objective and repeatable for a statistically significant sample of data.

Regions were rejected for a number of reasons, primarily data gaps (in either MDI at or near the emergence time, or GONG data for final analysis) or immediate proximity (within the 128×100 pixel box) of another active region. No further tests were made concerning the eventual size of the active region

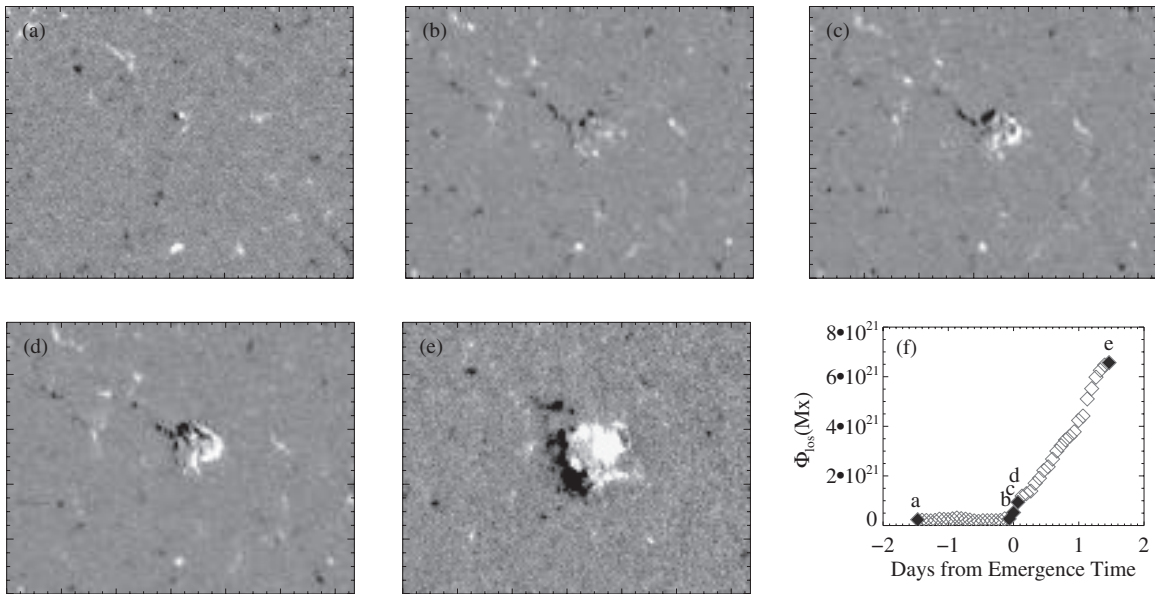


Figure 2. Example of a pre-emergence target, NOAA AR 10559, which had an assigned emergence time t_0 of 2004-02-13T11:15:02.677Z (see the text for details) at N07 W22.4. The images (a–e) are the 128×100 pixel images from the MDI full-disk line-of-sight magnetic data used for initial evaluation of the emergence episode, all scaled to ± 500 G. The image (c) shows the assigned “emergence time” t_0 . The temporal evolution of the pseudo-flux $\Phi_{\text{los}} = \sum |B_{\text{los}}|/\mu \Delta A$ for this test field of view is shown in (f), as a function of time relative to the inferred time of emergence, determined as the first MDI magnetogram when 10% of the eventual maximum change in flux, Φ_{los} , has appeared (c). Data points for the images shown are filled in and labeled; a mix of 30 s and 300 s MDI data are both used and shown here, evident by the different apparent noise levels.

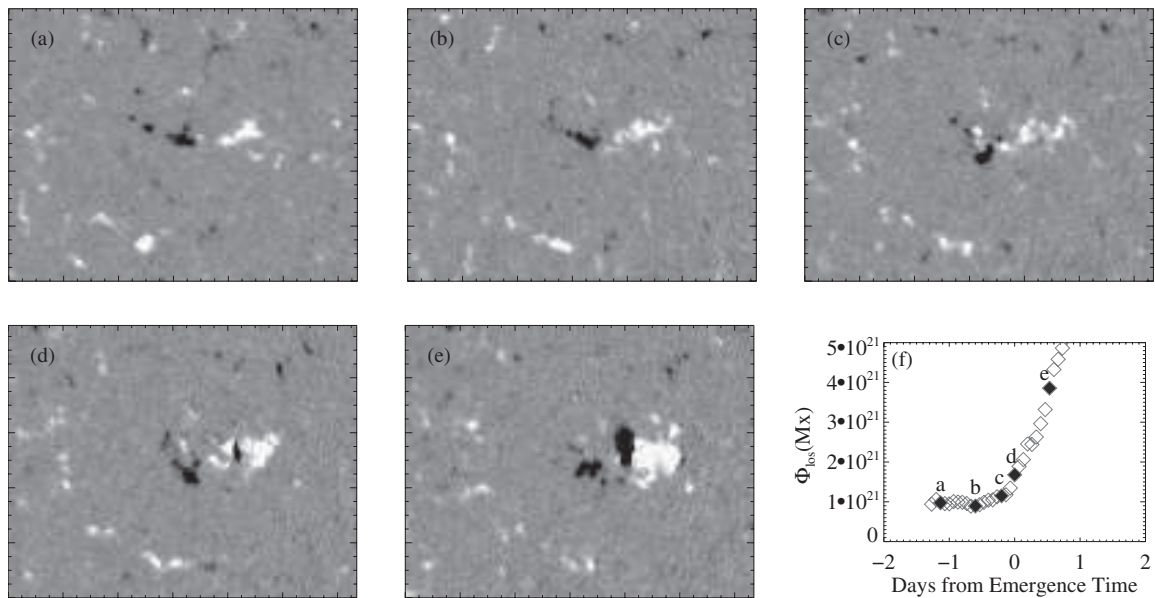


Figure 3. Example of a pre-emergence target with a less-clear emergence time, NOAA AR 9564, which had an assigned emergence time t_0 of 2001-08-01T06:27:01.250Z (see the text for details) at N14 W21.2. The images (a–e) are in the same format as in Figure 2. The temporal evolution of Φ_{los} is shown in (f), except that the maximum flux observed is truncated to better show the early evolution. Data points for the images shown are filled in and labeled. In this case, the “background” $\Phi_{\text{los}} = 0.96 \times 10^{21}$ Mx is larger than the previous example. The region eventually reached 9.5×10^{21} Mx, or a maximum increase of 8.6×10^{21} Mx, hence point (d) at 1.8×10^{21} Mx was the identified emergence time by the objective algorithm. However, it is clear that a small episode of flux emergence apparently occurred between (b) and (c) as well. While in this case we can argue a 6 hr uncertainty in the emergence times, there was very little if any surface signal of the emergence for many hours prior to (c).

or speed of emergence; a later subjective evaluation rejected regions if t_0 appeared incorrect by more than a few MDI-derived data points. The fixed box used at this stage was fairly restrictive.

The refined location and time of emergence, defined as above, were used to generate the Doppler-velocity data (see Section 3.4). The final result is 107 pre-emergence (“PE”) target regions between 2001 and 2007. In Table 1, we list the

identifying features of these regions: the NOAA active region number, the t_0 as defined above, and the latitude and longitude of the center of the 128×100 pixel box at that time. Note that the longitude was generally refined from the NOAA reports, while the latitude generally was not, and as such is effectively an integer. In Figure 4, we show the final distribution of the (eventual) maximum size achieved (as reported in the NOAA compilations) for the active regions in the PE list.

Table 1
Identifying Coordinates for Pre-emergence Targets

Region	Emergence	Location ($^{\circ}$)		Max Size (μH)
		ID	Date “ t_0 ”	Latitude
9559	2001 Jul 27 04:51	–26.0	–30.0	50
9564	2001 Aug 1 06:27	14.0	21.2	130
9567	2001 Aug 2 16:03	–15.0	–21.2	100
9579	2001 Aug 13 11:11	–18.0	–15.1	60
9645 ^a	2001 Sep 30 12:47	–19.0	–28.2	210
9651	2001 Oct 3 16:03	–23.0	–9.4	50
9652	2001 Oct 4 06:23	23.0	–28.9	20
9693	2001 Nov 7 08:03	11.0	–17.6	60
9725	2001 Dec 1 14:27	–11.0	20.0	80
9729	2001 Dec 4 17:36	24.0	–26.5	50
9739	2001 Dec 13 11:15	–13.0	–10.6	520
9746	2001 Dec 19 03:11	–16.0	–25.1	30
9770	2002 Jan 1 19:15	7.0	7.0	90
9791	2002 Jan 19 17:36	–4.0	3.7	140
9812	2002 Feb 2 06:24	12.0	0.4	50
9841	2002 Feb 22 01:36	–21.0	1.9	110
9854	2002 Mar 2 09:36	10.0	–17.7	30
9858	2002 Mar 3 12:48	–29.0	–30.4	60
9873	2002 Mar 15 20:48	–17.0	–26.9	130
9877	2002 Mar 20 03:12	18.0	11.1	260
9894	2002 Apr 3 14:24	15.0	–27.9	30
9897	2002 Apr 6 01:36	–1.0	–13.9	100
9908	2002 Apr 11 19:12	5.0	3.4	70
9924	2002 Apr 23 17:36	–17.0	–15.4	70
9976	2002 May 29 04:48	–11.0	–31.2	30
9993	2002 Jun 8 17:35	7.0	2.0	50
10006	2002 Jun 17 15:59	–8.0	0.4	30
10021	2002 Jul 2 07:59	–29.0	–33.2	120
10040	2002 Jul 22 01:36	–23.0	–19.2	20
10049	2002 Jul 25 20:47	–6.0	8.7	30
10057	2002 Jul 31 16:03	–9.0	–24.7	450
10060	2002 Aug 2 17:36	–29.0	2.9	50
10078	2002 Aug 13 14:27	–11.0	–12.4	100
10132 ^a	2002 Sep 21 16:03	19.0	–22.1	470
10135	2002 Sep 26 11:12	–27.0	–32.0	60
10152	2002 Oct 10 01:35	20.0	2.0	20
10186	2002 Nov 4 12:48	19.0	–28.0	60
10192	2002 Nov 11 03:11	13.0	–26.1	630
10193	2002 Nov 12 06:27	–2.0	–36.7	20
10219	2002 Dec 6 11:12	–8.0	–31.7	30
10232	2002 Dec 20 14:27	13.0	–17.1	20
10253	2003 Jan 10 04:47	11.0	18.7	70
10273	2003 Jan 26 20:47	6.0	2.4	160
10292	2003 Feb 24 19:14	–8.0	–8.4	150
10298	2003 Mar 3 03:11	–9.0	–35.2	40
10317	2003 Mar 19 09:39	4.0	–29.7	30
10328	2003 Mar 30 08:03	–11.0	–33.7	10
10327	2003 Mar 31 08:03	–7.0	2.7	40
10331	2003 Apr 4 20:48	–7.0	–13.0	50
10359	2003 May 11 20:47	–16.0	3.3	20
10417	2003 Jul 19 04:46	–20.0	6.0	600
10423	2003 Jul 31 04:47	–19.0	–12.1	20
10427	2003 Aug 2 19:12	3.0	–7.0	110
10428	2003 Aug 4 04:51	17.0	6.0	60
10439	2003 Aug 20 20:47	8.0	3.0	70
10443	2003 Aug 24 06:23	22.0	4.8	20
10453	2003 Sep 3 08:03	–23.0	15.0	260
10461	2003 Sep 14 12:48	12.0	1.3	270
10462	2003 Sep 14 22:24	–9.0	3.7	90
10480	2003 Oct 14 16:03	20.0	2.0	50
10481	2003 Oct 16 12:47	–8.0	–7.9	40
10488 ^a	2003 Oct 26 11:11	8.0	–32.7	930
10492	2003 Oct 26 17:35	–22.0	2.2	360
10498 ^a	2003 Nov 8 00:03	–3.0	7.0	240

Table 1
(Continued)

Region	Emergence	Location ($^{\circ}$)		Max Size (μH)
		ID	Date “ t_0 ”	Latitude
10500	2003 Nov 8 20:47	–8.0	1.3	40
10503	2003 Nov 15 09:35	18.0	–21.7	20
10522	2003 Dec 11 11:11	15.0	8.9	50
10529	2003 Dec 18 22:23	9.0	–17.2	20
10532	2003 Dec 23 22:15	–11.0	–36.2	70
10543	2004 Jan 19 08:03	–18.0	–19.6	110
10550	2004 Jan 31 20:47	–8.0	–21.2	40
10553	2004 Feb 3 14:23	–6.0	–36.5	40
10559 ^a	2004 Feb 13 11:15	7.0	15.7	80
10568	2004 Feb 26 20:47	–17.0	–13.5	30
10591	2004 Apr 11 14:27	–15.0	–25.7	100
10602	2004 Apr 28 22:23	–14.0	19.7	60
10601 ^a	2004 Apr 29 14:23	–9.0	5.3	310
10605	2004 May 3 12:47	–12.0	–24.7	130
10619	2004 May 23 01:36	–9.0	18.5	30
10623	2004 Jun 1 00:03	7.0	3.9	70
10626	2004 Jun 4 19:12	5.0	–16.2	20
10643	2004 Jul 8 15:59	–8.0	–16.4	30
10645	2004 Jul 9 03:11	12.0	–26.2	20
10671 ^a	2004 Sep 6 08:03	–10.0	13.6	540
10688	2004 Oct 19 06:27	–7.0	16.6	170
10737	2005 Feb 23 03:15	–9.0	12.5	50
10753	2005 Apr 12 14:27	12.0	–18.2	20
10757	2005 Apr 27 15:59	–5.0	–27.2	110
10770 ^a	2005 May 28 23:59	12.0	–17.1	70
10771	2005 May 29 12:47	24.0	8.0	50
10829	2005 Dec 2 04:48	11.0	–18.7	40
10839	2005 Dec 20 11:15	18.0	–30.0	40
10846	2006 Jan 14 06:27	4.0	1.1	140
10850	2006 Jan 22 11:12	6.0	–21.6	30
10852	2006 Feb 6 22:24	–10.0	–28.7	20
10868	2006 Apr 4 07:59	–7.0	–21.9	40
10889	2006 May 27 09:39	–3.0	–21.4	60
10890	2006 May 27 22:24	–14.0	7.6	50
10902	2006 Jul 30 01:36	–9.0	12.5	50
10916	2006 Oct 9 06:24	–13.0	–22.2	30
10919	2006 Oct 27 03:11	–16.0	–17.7	20
10937	2007 Jan 7 11:11	–13.0	–33.2	50
10939 ^a	2007 Jan 19 22:27	–3.0	4.2	180
10964 ^a	2007 Jul 12 09:35	4.0	0.4	90
10971	2007 Sep 27 09:35	6.0	–35.4	70
10972 ^a	2007 Oct 5 12:51	–6.0	–20.7	70
10974	2007 Nov 15 20:51	12.0	–15.9	40

Note. ^a Member of the “Ultra-Clean” subset.

A subset of 11 regions is singled out as being particularly “clean,” and these regions are indicated with a superindex “a” in Table 1. The criteria for this list are completely subjective: no neighboring active region in the extracted areas, a very flat pre-emergence flux history, and an emergence characterized by a very uniform and steep slope of $d\Phi_{\text{los}}/dt$. The example shown in Figure 2 is one such member of the “Ultra-Clean subset.”

3.2. Target Selection Criteria: The “NE”s: No-emergence Control Regions

The active-region emergence targets required an accompanying set of “control data.” As our final analysis is a statistical analysis based on the results of both helioseismology-derived and magnetic-derived parameters, the control data needed to be constructed so as to not introduce statistical bias into the final distributions. We outline the construction of this data set here.

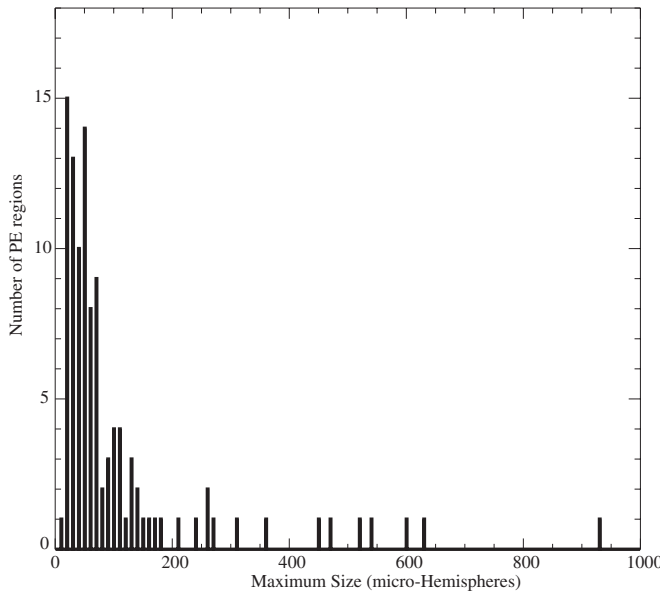


Figure 4. Histogram of the maximum size of the sunspot group attained during disk visibility of the emerging active regions, in μH (micro-hemispheres), as reported by the NOAA active-region lists. The minimum reported size is $10 \mu\text{H}$; the largest included in this sample was $930 \mu\text{H}$.

Starting every two MDI days during the same 2001–2007 interval, using the same-sized 128×100 pixel tracked boxes, areas were identified where the underlying signal stayed consistently $<1000 \text{ G}$.⁶ This was accomplished by “stacking” three days’ worth of MDI data and extending the target box to effectively cover the tracked area, as shown in Figure 5. Random locations for these low-field areas were chosen on the disk for each stack, subject to the same general constraints as the PE targets with regards to limits on latitude and longitude. A time close to the center of the 3 day interval, falling on an MDI observed time, is designated t_0 for the no-emergence (NE) data. While there was the possibility of overlapping areas being chosen, any randomly selected NE patch which did overlap was “weeded out” as described below. An example of a “no-emergence” region is shown in Figure 6.

This selection algorithm initially provided thousands of possible NE targets over the 7 years. A subset of approximately 500, selected to generally follow the distribution in latitude, longitude, and time as the initial set of PE targets, were used to acquire GONG data (see Section 3.4).

From these, a subjective evaluation was made, removing approximately 20 targets from consideration primarily due to the existence of small (obviously, un-numbered) emerging flux regions at the center of the field-of-view which were not previously detected. While no specific criteria were used regarding increasing or changing total flux over the time interval, the single criterion specified above effectively performed to constrain selection to regions with impressively consistent magnetic flux levels, on the whole.

Candidate NE regions were further evaluated and removed if the central $16^\circ \times 16^\circ$ (used for the majority of the helioseismology analysis, see Section 3.4) overlapped with the central $16^\circ \times 16^\circ$ portion of a PE or another NE at any time. The final number of NE controls available for distribution control (see Section 3.3, below) was 308.

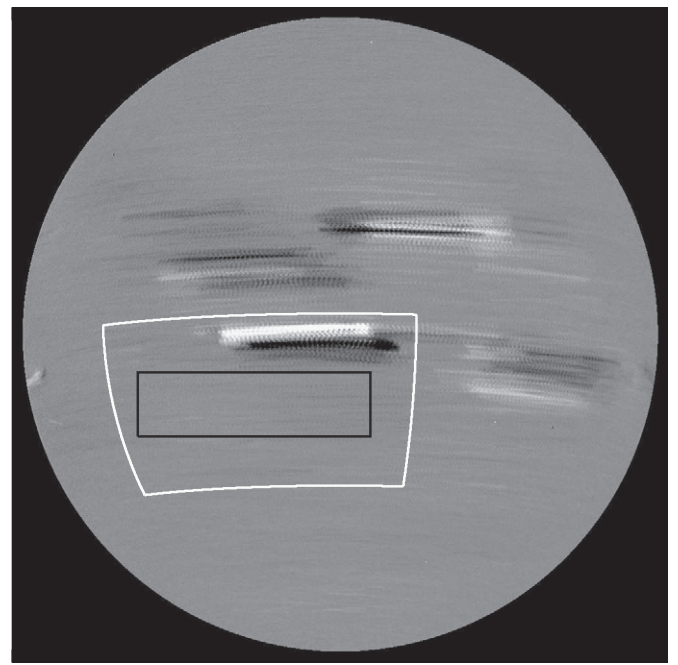


Figure 5. Selection area and eventual data-extraction area of a non-emergence target. Three days of MDI 96 minute data beginning with MDI orbit 4053 (2004-02-06T00:03:02.469Z) have been averaged together and shown here scaled to $\pm 100 \text{ G}$. The black box shows the coverage of a 128×100 pixel box tracked over the three days, indicating the entire quiet or “Non-emerging” (“NE”) area that consistently has only signal $<1000 \text{ G}$ over the three days. The white box indicates the area of tracked GONG and MDI data eventually used for the full analysis, discussed in Sections 3.4 and 3.5.

3.3. Distribution Control

An algorithm was developed for post-facto selection from a larger sample of controls (NE) to match the distribution of the targets (PE) simultaneously in latitude, longitude, and time. A non-parametric density estimate (NPDE; e.g., Silverman 1986), using the Epanechnikov kernel and the optimal smoothing parameter for a normal distribution, was used to estimate the probability density function for the three variables on a regular grid in longitude, latitude, and $\ln(\text{time})$ (see Figure 7). The non-parametric approach was used to avoid misrepresenting non-Gaussian distributions such as the latitude of emergence (which is decidedly and expectedly double peaked); similarly, the logarithm of the time variable⁷ was used to compensate for its extremely skewed distribution. A simulated annealing algorithm (e.g., Press et al. 1992; Metropolis et al. 1953; Kirkpatrick et al. 1983) was employed to select the subset of NE of a specified size (equal to the number of PE) that minimizes the integrated absolute value of the difference between the two NPDEs (NE and PE). Using the integral preserves the general shapes of the distribution rather than (for example) employing a peak or maximum difference as a Kolmogorov–Smirnov test would do.

The results of this matching exercise are shown for the three variables in Figure 7. A table listing coordinates for the final NE targets is provided in Table 2, where we list the MDI orbits generally containing the NE region, the mid-point of the GONG day used for analysis (see Section 3.4, below), and the coordinates of that mid-point (note we do not list t_0 precisely, but it is fairly inconsequential).

⁶ Gauss are used as units, with the understanding it is a pixel-averaged quantity.

⁷ Specifically, the logarithm of the number of Julian days since 2001 July 25, two days before the first data set.

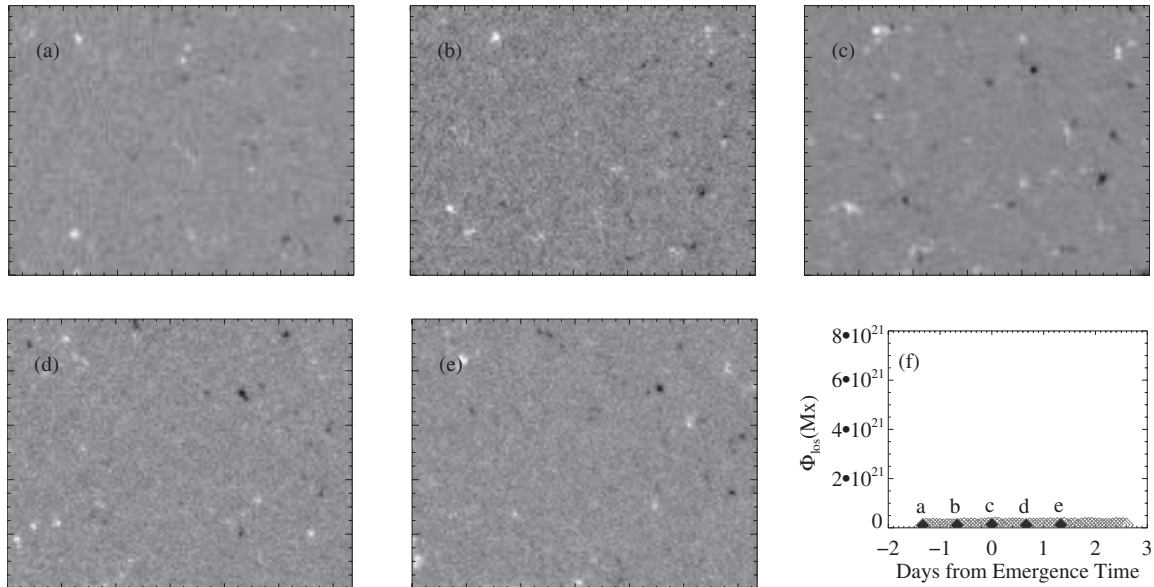


Figure 6. Non-emergence target from Figure 5, which had an assigned center time t_0 of 2004-02-07T08:03:02.501Z (see the text for details) at S18.6 E17.4. The images (a–e) are the 128×100 images from the MDI full-disk line-of-sight magnetic data used for initial evaluation of the emergence episode, all scaled to ± 500 G. The temporal evolution (f) of the pseudo-flux $\sum |B_{\text{los}}| / \mu \Delta A$ for this test field of view, as a function of time relative to the inferred time of emergence, scaled to match Figure 2. Data points for the images shown are filled in and labeled.

The equal sample sizes of PE targets and NE controls impose a specific requirement on the statistical tests: the prior probabilities, of which type of event (PE or NE) is more or less frequent, is set to be equal. This statistical requirement is maintained even after a further restriction is placed on the data for acceptable GONG duty cycle (see Section 3.4 and Table 3) which in fact creates small inequities in the sample sizes. With equal prior probabilities, the goal of determining whether these populations differ is emphasized. Were this a test of prediction, the sample sizes (hence prior probabilities) should reflect the chances of any random place on the Sun being a location and time of emergence; clearly this is a ratio of many thousands to one.

3.4. Preparing the Doppler-velocity Cubes

After the appropriate target selection, there is no difference in the treatment of the PE and NE data cubes produced from the GONG Doppler-velocity data. Cubes $32^\circ \times 32^\circ$ in extent were tracked at the Carrington rate and extracted from the GONG 1 minute velocity data (Corbard et al. 2003). As indicated in Figures 1 and 8, this extracted area is larger than the original 128×100 MDI-pixel area used for initial evaluation.

The final cubes used for this analysis are one “GONG-day” long (1664 minutes); for the PE data, the cubes end 16 minutes after the emergence time t_0 due to a small communication error; given the temporal sampling of the magnetic field data, we do not assign significance to the 16 minutes aside from assuming there will be early emergence magnetic flux appearing near the end of the GONG day.

The extracted Doppler-velocity data are re-projected using a Postel projection (Pearson 1990). The 1664 minute time series are then broken into five time intervals, each 384 minutes long but starting every 320 minutes (thus an overlap of 64 minutes between each interval). A schematic of the data and the temporal relationship between time intervals is shown in Figure 9.

The GONG facility includes different observing sites whose data are combined to create full temporal coverage. While the average duty cycle for GONG data is very high, at times the

coverage falters for a variety of reasons. Intervals that fall below a duty cycle of 80% are not included in the analysis. This restriction removes data randomly; there is no reason for duty cycle to be tied to PEs preferentially over NEs, especially after the matching was performed for location and date. In addition, what are removed from consideration are individual intervals rather than an entire PE or NE target. Table 3 presents the resulting sample sizes for PE and NE populations by interval, after removing data with insufficient duty cycle.

3.5. The Accompanying Magnetic Data for Analysis

In addition to the considering each event (or lack thereof) as viewed by helioseismology, to confirm that the results are a result of subsurface processes, we produced a complementary data set of the surface field. For analysis we attempt to mitigate projection effects present due to the fact that the MDI data detect only the line-of-sight component of the flux density (explained in detail below). We also want to match the measure of the surface magnetic field to the area and projection used with the GONG Doppler-velocity data cubes. To achieve this, first the location and $32^\circ \times 32^\circ$ spatial extent of the GONG cubes were identified in MDI data covering the same time interval.

To minimize projection effects and, more adroitly, use the most physically meaningful magnetic measure available from the MDI data, we use a potential-field calculation to retrieve an estimate of the radial component of the field. Specifically, the potential field was calculated to directly match the observed line-of-sight boundary (Sakurai 1982; Bogdan 1986; Rudenko 2001), rather than assuming the boundary was equivalent to the radial component of the field.

In general, the radial component of a potential field (without a source surface) in the volume above the solar surface can be expressed in a spherical harmonic expansion as

$$B_r(r \geq R_\odot, \mu, \phi) = \sum_{l=1}^{\infty} \sum_{m=0}^l (l+1) \left(\frac{R_\odot}{r} \right)^{l+2} \times [g_l^m \cos m\phi + h_l^m \sin m\phi] P_l^m(\mu), \quad (1)$$

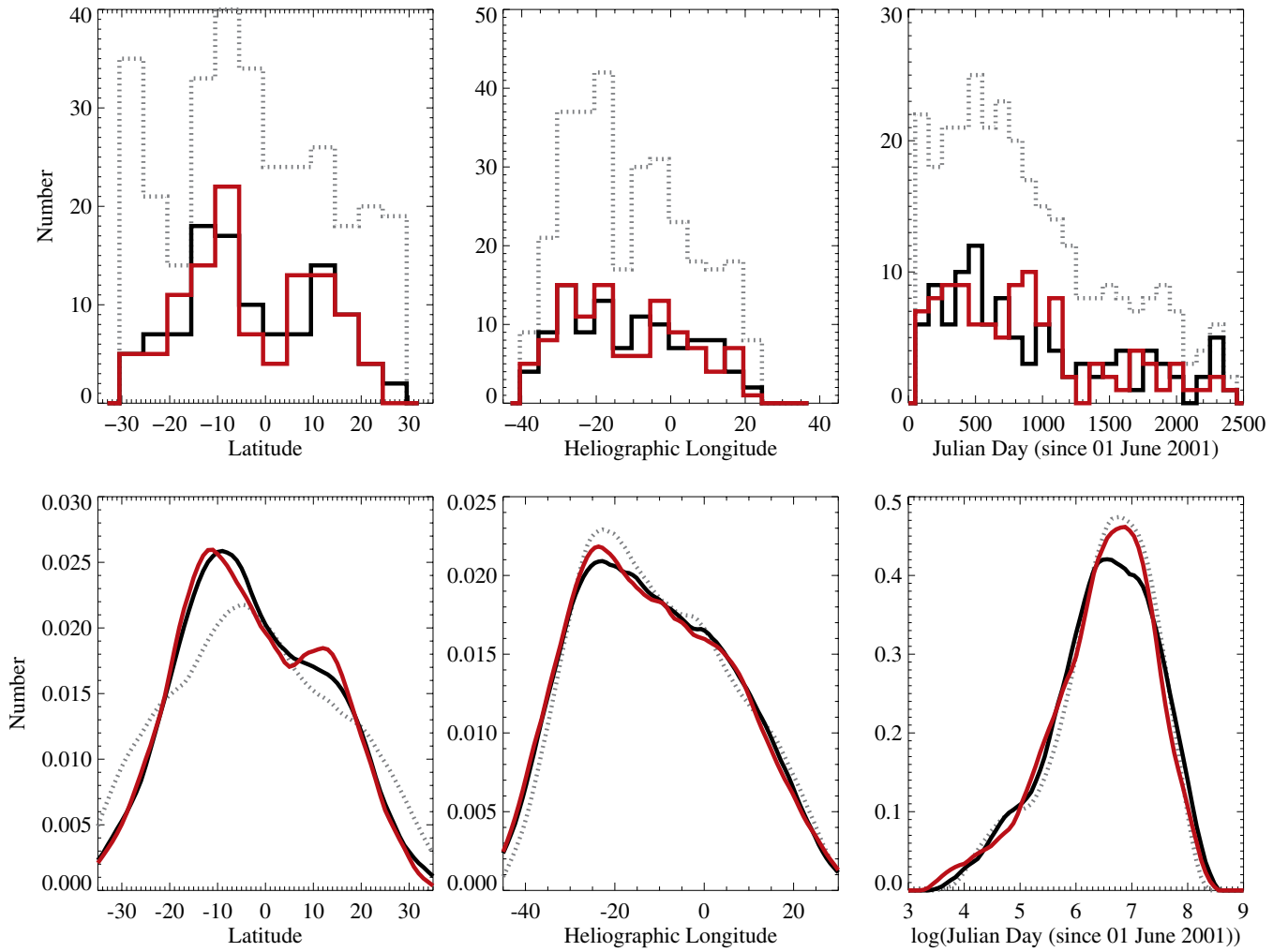


Figure 7. Distributions of latitude (left), heliographic longitude (center), and date (right) at t_0 , the defined emergence time. Shown are the PE distributions (red), the larger sample of NE data (black, dotted) from which the matching algorithm drew the final sample (black, solid) which minimized the integrated difference between the PE and NE non-parametric density estimates (NPDE) of the three quantities simultaneously. Top row: histograms of the relevant quantities, hence indicating number in each bin; bottom row: the NPDE distributions, on which the minimization was performed. The one-dimensional matches (one variable at a time) are shown here, whereas the optimization was performed on all three variables simultaneously. Hence, while better one-dimensional matches may certainly be obtainable, it would be at the cost of the three-dimensional match results.

where the P_l^m are the associated Legendre functions, R_\odot is the solar radius, r is distance from the center of the sun, θ is co-latitude, and ϕ is longitude (measured for any choice of the polar axis). Following the approach of Rudenko (2001) by taking the polar axis of the coordinate system to lie along the line of sight, and using relationships among the associated Legendre functions as done by Bogdan (1986), the coefficients can be written as

$$g_l^m = \frac{(2l+3)(l-m)!}{4\pi(l+m+1)!} \int_0^1 d\mu \times \int_0^{2\pi} d\phi \cos m\phi P_{l+1}^m(\mu) B_l(R_\odot, \mu, \phi) \quad (2)$$

and

$$h_l^m = \frac{(2l+3)(l-m)!}{4\pi(l+m+1)!} \int_0^1 d\mu \times \int_0^{2\pi} d\phi \sin m\phi P_{l+1}^m(\mu) B_l(R_\odot, \mu, \phi), \quad (3)$$

where $B_l(R_\odot, \mu, \phi)$ is the line-of-sight component of the field at the solar surface. To ensure that the monopole term vanishes in the sum, we further assumed that the field on the far side of the Sun was given by $B_l(R_\odot, \pi - \theta, \phi) = B_l(R_\odot, \theta, \phi)$, where the front side of the Sun is assumed to lie in the range $0 < \theta < \pi/2$. This can produce some unphysical results very close to the limb, but does not greatly affect the field at the surface in the restricted area of the disk considered in this investigation. The integrals were evaluated using a simple trapezoid method, and the spherical harmonics were computed using the freely available software archive SHTOOLS,⁸ which have a relative error of less than 10^{-5} up to degrees of at least 2600. However, only terms up to degrees of 1000 were included, as this is sufficient to reconstruct spatial scales on the order of the resolution of MDI. Note also that the acoustic modes in the GONG data are seen up to about $l = 1000$ (see Figure 1 from Birch et al. 2012).

The above calculations were performed on an extracted cube slightly larger than $32^\circ \times 32^\circ$, then the potential field radial component was subjected to Postel projection and trimmed to

⁸ Available at <http://www.ipgp.fr/~wieczor/SHTOOLS/SHTOOLS.html>.

Table 2
Identifying Coordinates for No-emergence Targets

Region ID (MDI Orbit)	GONG-Day Reference Date	Reference Location (°)	
		Latitude	Longitude
3137-3140	2001 Aug 5 07:11	-4.5	-26.9
3148-3151	2001 Aug 16 08:48	-13.3	-11.4
3154-3157	2001 Aug 22 10:23	-26.5	-19.4
3175-3178	2001 Sep 12 00:51	27.6	-29.5
3177-3180	2001 Sep 13 19:59	-15.6	-26.4
3216-3219	2001 Oct 23 08:47	16.0	-14.1
3225-3228	2001 Nov 1 07:15	-15.8	-32.9
3226-3229	2001 Nov 2 00:51	-20.6	12.2
3232-3235	2001 Nov 8 02:27	-6.7	13.6
3234-3237	2001 Nov 10 07:11	0.2	-3.0
3249-3252	2001 Nov 25 00:51	0.7	-23.5
3257-3260	2001 Dec 2 13:39	18.5	16.7
3277-3280	2001 Dec 23 00:47	-23.9	-9.7
3283-3286	2001 Dec 29 10:23	25.2	-21.1
3304-3307	2002 Jan 19 04:00	-26.7	-28.0
3355-3358	2002 Mar 10 15:15	-14.9	-18.2
3369-3372	2002 Mar 25 04:00	18.7	-9.0
3372-3375	2002 Mar 27 16:48	-4.4	-35.0
3405-3408	2002 Apr 29 18:23	-24.1	-25.2
3415-3418	2002 May 10 00:47	5.6	11.1
3418-3421	2002 May 13 02:22	15.6	-19.2
3430-3433	2002 May 25 02:24	-2.3	-6.0
3455-3458	2002 Jun 18 16:51	-8.9	-17.2
3456-3459	2002 Jun 20 08:48	-21.1	-13.0
3471-3474	2002 Jul 5 02:27	14.5	-2.6
3472-3475	2002 Jul 5 13:35	12.0	-23.1
3479-3482	2002 Jul 13 08:47	-1.4	3.0
3484-3487	2002 Jul 18 02:23	-29.0	2.8
3502-3505	2002 Aug 4 18:23	-21.9	-10.7
3508-3511	2002 Aug 11 00:47	-11.4	-21.4
3519-3522	2002 Aug 22 02:27	3.7	0.4
3535-3538	2002 Sep 7 05:35	-8.8	-36.2
3547-3550	2002 Sep 19 02:23	12.9	-29.0
3555-3558	2002 Sep 27 00:48	-13.7	-33.2
3555-3558	2002 Sep 27 02:24	15.3	7.9
3564-3567	2002 Oct 5 11:59	-6.0	-0.1
3565-3568	2002 Oct 7 00:51	-18.7	-22.9
3597-3600	2002 Nov 8 07:11	-29.4	-32.7
3600-3603	2002 Nov 11 10:24	-4.5	-12.8
3607-3610	2002 Nov 17 16:51	11.0	-17.7
3607-3610	2002 Nov 18 07:15	6.2	7.3
3611-3614	2002 Nov 22 05:36	10.4	8.5
3615-3618	2002 Nov 26 02:27	-13.2	-2.0
3636-3639	2002 Dec 17 04:03	2.8	-35.9
3646-3649	2002 Dec 27 08:48	-12.5	-2.7
3683-3686	2003 Feb 2 11:59	17.1	-27.6
3694-3697	2003 Feb 13 05:35	11.2	-6.7
3703-3706	2003 Feb 21 18:26	-7.7	5.9
3703-3706	2003 Feb 21 20:02	-10.1	-11.2
3753-3756	2003 Apr 12 18:23	-6.6	-8.5
3758-3761	2003 Apr 18 08:47	-5.9	-25.4
3780-3783	2003 May 10 07:11	-15.8	9.0
3782-3785	2003 May 11 18:22	-13.1	-27.2
3789-3792	2003 May 19 05:35	-5.4	-7.5
3795-3798	2003 May 24 19:59	24.6	-3.6
3802-3805	2003 May 31 11:59	-20.7	-33.0
3810-3813	2003 Jun 9 08:47	-27.6	12.6
3855-3858	2003 Jul 24 02:22	23.2	-27.7
3863-3866	2003 Jul 31 13:35	-7.6	17.9
3874-3877	2003 Aug 12 02:27	7.9	1.0
3893-3896	2003 Aug 30 15:15	10.3	-32.5
3910-3913	2003 Sep 16 21:36	15.7	-4.5
3969-3972	2003 Nov 14 23:11	18.4	11.1
3983-3986	2003 Nov 28 21:39	0.3	-31.1
3997-4000	2003 Dec 12 15:15	-12.9	1.5

Table 2
(Continued)

Region ID (MDI Orbit)	GONG-Day Reference Date	Reference Location (°)	
		Latitude	Longitude
4043-4046	2004 Jan 28 00:47	-8.4	16.4
4044-4047	2004 Jan 29 07:11	14.5	-17.5
4053-4056	2004 Feb 6 20:03	-18.6	-23.9
4067-4070	2004 Feb 20 15:12	-16.7	13.1
4073-4076	2004 Feb 26 16:47	15.8	-16.9
4084-4087	2004 Mar 8 21:39	1.6	-25.9
4138-4141	2004 May 1 13:35	-11.8	-19.7
4157-4160	2004 May 20 18:24	-7.3	-30.5
4176-4179	2004 Jun 8 13:39	21.4	11.2
4217-4220	2004 Jul 19 16:47	6.4	-7.0
4228-4231	2004 Jul 30 23:11	-17.0	-5.9
4256-4259	2004 Aug 27 15:11	-10.7	-16.2
4327-4330	2004 Nov 7 10:23	-13.6	-16.2
4334-4337	2004 Nov 13 13:35	-7.4	20.1
4404-4407	2005 Jan 23 00:47	-6.2	2.3
4441-4444	2005 Feb 28 15:15	3.6	-4.9
4518-4521	2005 May 17 07:12	-3.0	-29.1
4551-4554	2005 Jun 19 00:51	10.1	-24.2
4580-4583	2005 Jul 17 19:59	10.8	2.5
4604-4607	2005 Aug 10 13:35	10.2	-13.0
4623-4626	2005 Aug 29 15:11	-8.5	-25.2
4628-4631	2005 Sep 4 04:03	13.3	-17.5
4669-4672	2005 Oct 15 07:12	12.0	-18.5
4676-4679	2005 Oct 22 08:48	-5.2	-27.7
4733-4736	2005 Dec 18 07:12	11.8	-33.0
4833-4836	2006 Mar 28 02:23	-7.5	-9.5
4834-4837	2006 Mar 28 16:51	-11.8	-25.7
4913-4916	2006 Jun 15 21:35	-14.2	-23.1
4916-4919	2006 Jun 19 10:23	-23.9	-3.2
4929-4932	2006 Jul 2 05:36	-10.1	19.2
4955-4958	2006 Jul 27 20:03	-12.7	14.9
4959-4962	2006 Aug 1 00:51	-9.7	-20.4
5037-5040	2006 Oct 18 05:36	9.4	6.6
5113-5116	2007 Jan 2 00:51	-1.6	6.5
5233-5236	2007 May 1 12:03	5.0	22.2
5277-5280	2007 Jun 15 05:36	-2.2	-8.4
5335-5338	2007 Aug 11 12:03	24.7	-6.2
5374-5377	2007 Sep 19 19:59	8.6	-19.4
5384-5387	2007 Sep 30 02:23	-10.8	5.4
5397-5400	2007 Oct 12 15:11	-4.0	-1.4
5411-5414	2007 Oct 26 18:24	-3.5	-35.7
5472-5475	2007 Dec 26 18:27	-12.2	-34.7

Table 3
Duty Cycle for NE and PE Targets

Time Interval	NE Samples	PE Samples	Ultra-Clean PE Samples
TI-0	81	89	7
TI-1	85	88	10
TI-2	85	89	11
TI-3	82	87	9
TI-4	83	86	9

exactly match the GONG data cubes. Hence, we have for each PE and NE data set, a time series of the radial component of the field matched in area, and matched in projection, to subsurface observations made by helioseismology, albeit the latter by a different instrument.

From these maps, an appropriate time series of the history of the field at the target and its immediate surroundings is computed, for comparison with the results of helioseismology. Sample pairs of average radial field density and average

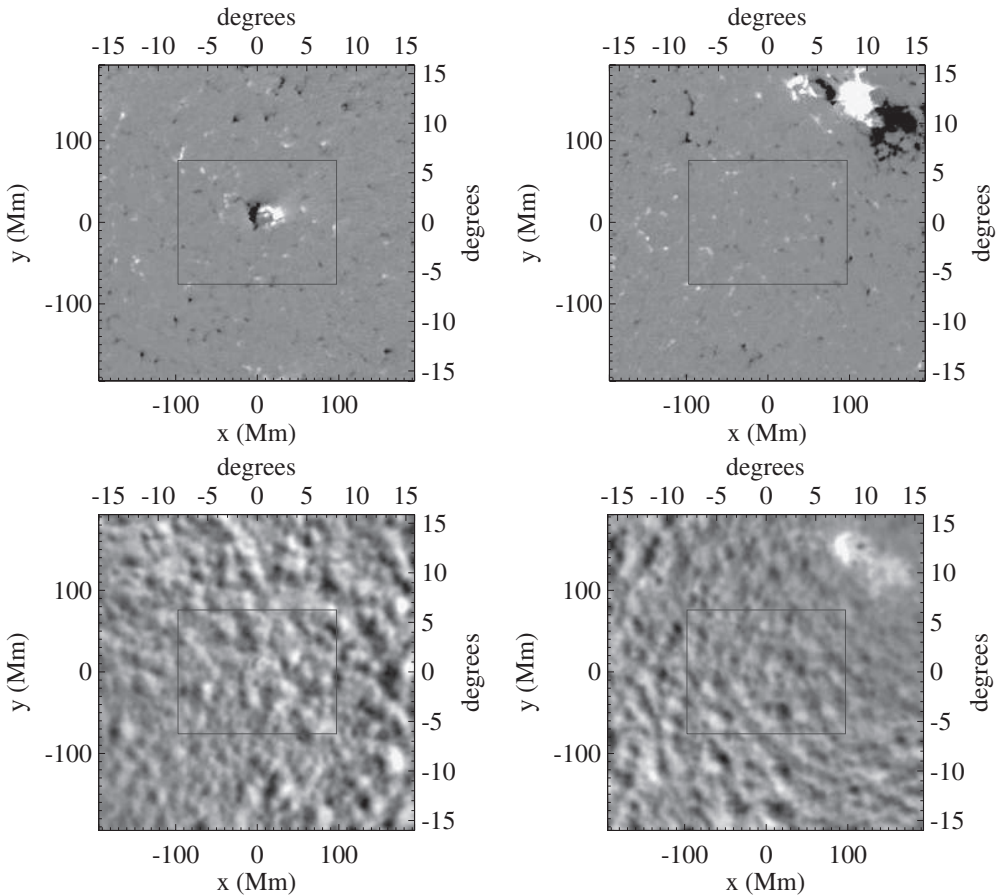


Figure 8. Top: the $32^\circ \times 32^\circ$ radial field image, matched to the GONG data area, for the same targets as Figures 2 and 6. Axes are shown in both Mm and degrees from the center tangent point. Left: average of the PE target AR 10559 2004 February 13 23:59–2004 February 14 06:23; Right: average NE target field 2004 February 7 01:35–08:03 UT. Bottom: average GONG Doppler images for the same targets, for 384 minutes each (the length of an interval used for the helioseismology analysis): left, for PE target AR 10559, for the same interval as the magnetogram average above; and right: for the NE target and the same interval. All images: gray boxes indicate the approximate area used for initial diagnostics (as in Figures 2 and 6) for reference, and as an explanation of the presence of significant magnetic flux, for example, in many NE targets.

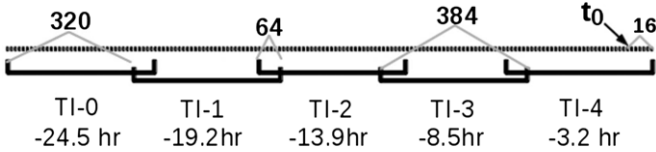


Figure 9. Schematic which demonstrates the temporal relationship of the time intervals. The dotted line represents the time series of GONG Doppler data, bold face numbers across the top are in minutes; the five time intervals are labeled “TI-#,” and the central time of each interval, in hours relative to the end of the GONG data, is indicated below its label. The GONG data run 1664 minutes, and end 16 minutes after the emergence time determined as described in the text. Intervals start every 320 minutes, are 384 minutes long, and overlap with neighboring intervals by 64 minutes. This schematic applies to both PE and NE data, albeit with a “fake” t_0 for the NE targets, which corresponds instead to exactly the end of the GONG data.

corresponding Doppler data are shown in Figure 8 for the PE and NE examples of Figures 2 and 6.

For these accompanying magnetic data, we show in Figure 10 the unsigned radial field averaged over all samples, for each of the time intervals used for the seismology analysis. To provide context, we extend this slightly in time and show the averages for two additional post-emergence time intervals. Of note is the distinct lack of variation in the NE data, but also the noticeable bands of stronger signal at the top and bottom of the NE data cubes compared to the central portion. The PE data show a distinct early signature of surface field 24 hr

prior to the emergence time, and a clear bipolar signature after emergence is underway. The bipolar structure is less clear but arguably present in the subset of PE data, the early signature is arguably completely absent when only the cleanest, “most virgin” examples were chosen. At the same time, averaging over a smaller number for the “ultra-clean” data set allows a single sample to influence the average: the strong persistent signal on the right-hand portion of the “ultra-clean” mean in Figure 10 is primarily due to a strong plage area near NOAA AR 9645.

3.6. Further Corrections

The latitude reported by NOAA was generally unchanged for extracting the GONG data cubes; the longitude was obviously updated according to t_0 . For the later analysis, especially the averages over all samples used in Birch et al. (2012), the coordinates were refined in the following manner. The time series of the radial magnetic field were used to construct bitmaps of new flux using the difference ($|\delta B|$) between the field roughly 12 hr after t_0 and the first time interval (roughly 24 hr before t_0), and only including in the bitmap areas where $|\delta B| > 0.3 \times \max(|\delta B|)$. A centroid was created from the resulting bitmap, and the coordinates were then assigned to be the location of this centroid.

In this manner, the analysis that is performed on averages taken over space, time, or sample will provide results that are not

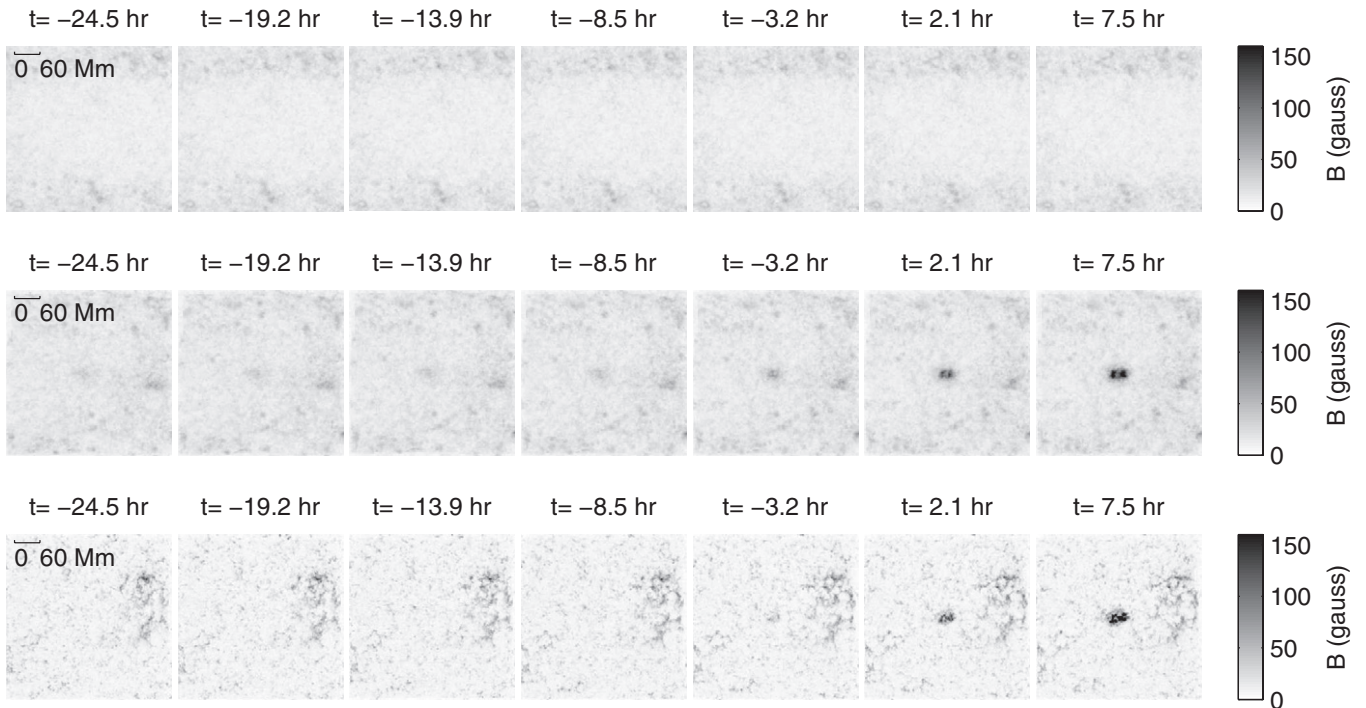


Figure 10. Averages over all samples of the unsigned radial field for each of the time intervals as accompanies the seismology data. In addition to the five primary intervals prior to emergence, we show here the averages for two additional intervals post-emergence, for comparison. Times indicate the central time of each interval, following Figure 9. All figures use the same gray scale. Top: the NE samples; middle: the PE samples; bottom: the “Ultra-Clean” subset of PE samples.

diluted by subtle differences in emergence location within the field of view. Accordingly, no similar refinement was performed for the NE samples, as there are no events by which to define such a refinement.

4. STATISTICAL CONTAMINATION ISSUES

This is a study trying to detect a small difference between two populations. How these populations are defined and the samples obtained, then, will directly affect the reliability of the results. The goal is that the PE regions be clear, distinct, isolated, and fairly near disk-center emergence episodes, and the NE regions be emergence-free episodes matched to the PE distributions in location and time (effectively, solar-cycle activity level) as described above.

Statistical contamination, the existence of a bias that will inadvertently identify the two populations without being directly related to the emergence process, may take a variety of forms. As alluded to in Section 2, we describe below our understanding of various contributions to possible contamination, and our efforts to mitigate them.

4.1. Nearby Field

Ideally, the background, nearby, or pre-existing field in the NE targets (their distribution in space, flux density, total flux, etc.) is indistinguishable from that of the PE targets prior to emergence. The emergence episodes and NE regions were initially characterized by 128×100 pixel tracked boxes in the MDI image-plane coordinate frame. The data cubes used for analysis were, as described above, $32^\circ \times 32^\circ$ on a heliographic grid. The difference between these two can be seen in Figure 8, and is not insignificant. The most noticeable effect is that the NE cubes in fact often contain stronger field at the periphery than the cutoff used to select the smaller areas (Figure 10). The PE cubes were isolated from nearby active regions in the original

128×100 pixel evaluation, but strong field (active regions) can be found in the larger $32^\circ \times 32^\circ$ field of view.

By comparing the signals averaged as shown in Figure 11, it is clear that there is a bias: the median signal of magnetic field is larger in the PE samples as compared to the NE samples. Note that by showing the median, rather than the mean, the results are not influenced by outliers and the distributions display a real difference. For the full $32^\circ \times 32^\circ$ field of view, the difference is significant but not large; when considering only the smaller central $16^\circ \times 16^\circ$, the PE sample result does not change noticeably (until emergence begins in the last time interval), whereas the NE sample median signal is quite reduced. This confirms that the initial 128×100 pixel evaluation area for the NE sample is “too quiet” compared to the enhanced signal in the NE sample peripheries and to the PE sample, even though the selection threshold was a generous 1 kG (Section 3.2).

The source of this bias may be introduced or it may be a real effect. The emergence really could start more than a day before t_0 , in which case there is no error, just a real physical effect only visible in the ensemble. However, by imposing a field strength limit on the NEs but not PEs, we may have introduced an artificial bias into the samples. Due to the matching in latitude and longitude, there should be no gross preferential prevalence of “background” field as there would be had all of the NE regions, for example, been selected outside the active latitudes or all in the same hemisphere. However, there was also no de-selection of PE candidates based on “active longitudes” (Petrovay & Abuzeid 1991; Gaizauskas et al. 1994; Pojoga & Cudnik 2002), and active longitude lifetimes are likely too short to be captured simultaneously in the time matching and longitude matching. If the bias is the effect of active longitudes, this is a real (solar) bias toward having pre-existing field for the PEs. The fact that the NEs are “too quiet” implies that the inconsistent use of a threshold contributes to the bias, but may not be the only effect. The significance of this

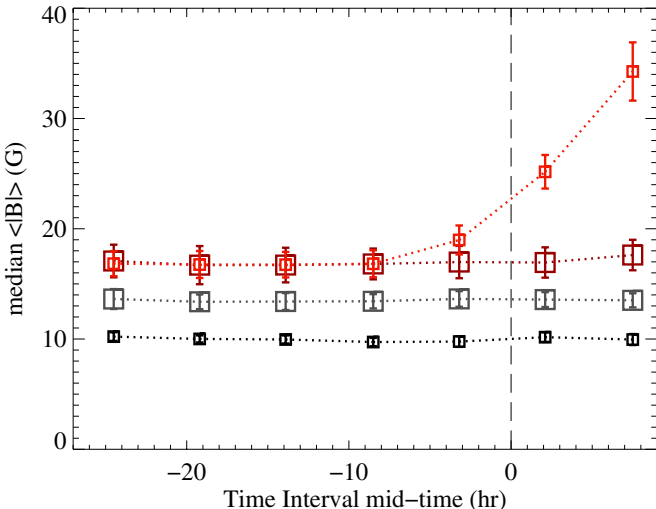


Figure 11. Median of the area-averaged unsigned field and the errors in the median (using a bootstrap method), for both the PE (red) and NE (black) data, plotted as a function of the central time of the intervals relative to the end of the GONG day (which is effectively t_0). Larger symbols (and muted red/gray) indicate that the median was taken over the entire extracted area, smaller (red/black) symbols indicate that only the smaller $\approx 16^\circ \times 16^\circ$ area used for the helioseismology analysis was included.

systematic difference between the samples is discussed in detail in Paper III.

4.2. Nearby or Short-lived Emergence

It is conceivable that nearby or ongoing short-lived flux emergence may contaminate the seismology signal we search for.

No screening or diagnostics was performed to specifically rule out nearby emergence episodes for either PE or NE samples. Both may have emerging flux regions in the periphery, and these data sets were not removed from consideration (as long as there were no emerging flux regions within the central $16^\circ \times 16^\circ$, or $\approx 100 \text{ Mm} \times 100 \text{ Mm}$). A variety of seismic analyses will be performed with varying pupil sizes (Birch et al. 2012), thus the influence of field in the sample peripheries can in fact be studied.

Very small-scale short-lived emergence episodes, “ephemeral regions” are ubiquitous and bring substantial flux to the solar surface (Harvey & Zwaan 1993; Hagenaar et al. 2003). The presence of ephemeral regions is not selected for or against, as their peak field strengths generally fall below the NE-selection threshold of 1 kG in MDI data, except one or two cases of removing an NE candidate due to a long-lived or especially large ephemeral region occurring at the center of the target. We make the assumption that the rate and distribution of ephemeral regions is the same between the samples of the NE and PE populations, and propose that no statistical bias is introduced due to the presence of ephemeral regions.

4.3. Misdetermination of Emergence Time

Numerous sources of error could lead to a misdetermination of t_0 , with effects presenting as bias or as random error.

The coarse temporal resolution MDI data used here could lead to a significant amount of “new” surface flux being present for an hour or so before the “emergence time” t_0 . The limited spatial resolution of the MDI data could lead to a significant amount of

undetectable flux being present for an unknown period before the “emergence time” t_0 . “Significant” is used here qualitatively, because it is the lack of data that is the primary source of the uncertainty itself. Lack of adequate sampling should add an element of random noise to comparisons between segments. The reliance on line-of-sight data, however, may present a systematic late determination of t_0 with respect to observing angle, since early flux emergence is signaled by horizontal field (Zwaan 1985; Zhang & Song 1992; Leka et al. 1996; Bernasconi et al. 2002; Kubo et al. 2003). In and of itself, the instrumental limitations should not present a statistical contamination between the NE and PE samples. Since the presence of surface field when none is expected (as due to the misdetermination of t_0) may impact the Doppler signal and hence the inferred helioseismic parameters, the results for the time interval comprising the last hours prior to t_0 will be interpreted with this uncertainty taken into account (Birch et al. 2012; Barnes et al. 2012).

Of a more subtle nature, in terms of this study, is the nature of flux emergence itself, the early evolution of active regions, and whether or how a very young active region is distinguishable from the general evolving magnetic background. While we employed an objective and quantitative method to determine t_0 , as needed for a statistical study, upon examination of any individual case, t_0 could be argued with. An example is shown in Figure 3. An area of unchanging plage is co-spatial with the eventual emergence of NOAA AR 9564, and episodes of small bipoles appearing are evident prior to t_0 upon detailed inspection. These bipoles would not gain attention beyond the numerous ephemeral regions continuously appearing on the surface (see Section 4.2) and indeed they did not gain NOAA’s attention, except that they were located where NOAA AR 9564 eventually appeared.

We hypothesize without further investigation that the pre-emergence surface-field signature in the all-PE averages (Figure 10) is an indication of this very common characteristic: pre-emergence field can be present, whether as remnant plage or very early emergence episodes that are unnotable in any individual PE time series. As commented on earlier, when only examples are selected for which—by visual inspection—there is no pre-emergence surface field, the PE field signature is reduced if not absent. A third option is that very early emerging flux is distributed and weak, and detectable only on average (Figure 10) with the MDI data due to the significantly reduced noise; in this case the pre-emergent surface-field signature is absent for the clean subset not due to their “ultra-clean” nature, but due to the smaller number of data sets being averaged, and hence the increased noise (compared to averages for all regions).

The impact of a varied flux-emergence rate on later analysis should be a source of noise but not statistical contamination. The rate of emergence of new flux was cited in Ilonidis et al. (2011) as a key parameter relating to the strength and timing of the PE signal. However, it does not bias the NE versus PE samples.

The final evaluation is that t_0 may be misdetermined by an amount comparable to the MDI 96 minutes sampling, hence the final time interval used for helioseismology analysis will be assumed contaminated by early emergence. Smaller episodes of new flux appearance are indistinguishable from that which routinely occurs over the solar disk without the subsequent formation of an active region, and can simply be considered a source of noise for the present analysis.

5. DISCUSSION

The tools of local helioseismology rightfully hold hope of sensitive and powerful diagnostics of the solar subsurface structure, evolution, and behavior. To interpret the helioseismic signals with physical insight, they must be isolated to those relevant to the events in question. To fruitfully make use of the signals, the full extent of bias and contamination must be understood. We have designed a study to examine what signatures prior to the appearance of solar active regions may be detected by local helioseismology tools and data at this time, and outlined the data selection criteria and preparation herein.

This study focuses on determining whether or not a seismology signal is evident prior to emergence and what its character might be. The goal is, as discussed in Section 1, inferring changes in the subsurface associated with active-region formation. Based on the preparation described here, in Birch et al. (2012) we report on average subsurface properties of the two samples (PE and NE) as derived using helioseismic holography, and find statistically significant signatures in average subsurface flows and wave speeds, but do not detect evidence of strong spatially extended flows in the top 20 Mm during the day preceding visible emergence. In Barnes et al. (2012), parameters are derived from the seismology and magnetic field to characterize each of the PE and NE regions, and discriminant analysis is used to measure differences between the sample sets. While statistically significant differences are found from this analysis, it is found that no single parameter can clearly distinguish a PE from an NE for any single region.

To mitigate sources of bias, the distributions of the samples are matched in location and time (epoch within the solar cycle). This approach is novel; however, PE areas are targeted here exactly because they *did* form an active region significant enough to be noticed by NOAA. The PE targets can thus be studied with respect to the *known* location and time of emergence, and the magnetic- and seismology-based analysis performed with respect to the target's *known* coordinates. There is a random component in the selection of the NE regions, but they, too, are selected with knowledge that no emergence occurred within a specific time interval. Hence, there is a bias in that we are pre-selecting targets for study according to what is known to have happened.

There is an intrinsic difference between this study design and any attempt at “forecasting” the emergence of an active region. A forecasting study would instead be required to sample all possible emergence sites and compare the signals to all other possible sites, without a priori knowledge aiding the analysis methods. At the very least, a study designed for forecasting must employ samples and statistics which reflect the prior probability of an active region emerging at a randomly selected place and time over the observable disk, which is extremely small. While the results presented in Birch et al. (2012) and Barnes et al. (2012), and the available “blind” data sets (see Section 5.2, below) may serve to guide later studies of the true forecasting ability of seismology for active-region appearance, we caution that study design and attention to prior probabilities are crucial to answering specific questions posed.

The present study uses a fairly large sample, and hence comparisons may be made to, e.g., Komm et al. (2009, 2011), even though the definition of “emerging” differs: here we focus on the period prior to any surface field while the Komm et al. studies included both new and growing active regions (with surface flux present). As such, the present study may be seen

as an extension of case studies which also focused on pre-emergence periods (e.g., Jensen et al. 2001; Ilonidis et al. 2011; Braun 2012) to statistically significant sample sizes, however, the methods and interpretive tools (depths, cadence, control samples if any) differ between these studies and the present one. We describe here the steps taken to acquire both the statistically significant sample size with a clear focus on pre-emergence phenomena (although see Section 5.1, below). With better tools and analysis approaches, the sometimes conflicting results in the literature should give way; then, only those effects which are truly specific to the emergence process will be the focus of discussion.

Any seismic changes detected prior to surface changes will be evaluated in the context of the predictions made by different theories covering the source and formation mechanisms of solar active regions. But the seismology is influenced by the early surface behavior, the interpretation of the surface behavior is influenced by our understanding of the emerging-flux scenarios, which is what we are trying to learn about using seismology. The analysis has a circularity to it which implies one thing most strongly: interpretation must be done with utmost care. Only then can model predictions be validated.

Emergence scenarios differ between active regions with respect to rate of flux increase, the existence of distinct emergence episodes, location with respect to remnant field, etc. As mentioned above, the early evolution of active regions is an active research area and distinctly tied to the subsurface behavior which is the focus of this study.

There are efforts underway (Martens et al. 2012) to perform automatic feature recognition on data from, for example, the instruments of *Solar Dynamics Observatory*. Combining emergence indications from HMI and AIA may be advantageous. Using such database of emergence times defined by an independent algorithm may lend objectivity to the results and ease of acquiring the larger samples we suggest, but it must be accompanied by research on the early evolution of active regions.

5.1. For Future Studies

Hindsight enables future improvement. The flaws of a study design become distinctly clear as the study progresses and “issues” arise; in the best situations the flaws can be remedied, but in many cases due to resource limitations, corrections or accommodations must be made mid-course. Specific effects that the flaws in the present study’s design had on the results will be discussed in Birch et al. (2012) and Barnes et al. (2012) as appropriate. Whereas this paper discusses the details of the design, the results also comprise the lessons learned over the duration of this study.

1. Characterizing early active-region appearance and evolution is very much a research topic. The (objective, independent) determination of emergence time and location should be performed using, ideally, vector magnetic field data to detect the earliest horizontal field (Section 4.3); vector data may thus alleviate any systematic bias in t_0 as a function of observing angle. Resolution issues aside, the early evolution of active regions may form a spectrum of behavior such that assigning a single location and time is in fact inappropriate. However, for a statistical study, the determination of emergence time must be performed, as we did here, in an objective and repeatable manner—recognizing that the answer is very sensitive to data resolution, sensitivity, and cadence.

2. Data selection rules must be applied to areas used in the final analysis with minimal discrepancies. As described in Section 3, the initial evaluation of the PE and NE regions was performed on a much smaller field of view than was eventually extracted from the GONG data (and than was also eventually extracted from the MDI data for magnetic-field comparisons). As such, there was more, and more varied, peripheral activity than was expected in both the NE and PE samples. The contamination is inevitable given the large number of active regions during solar maximum activity; still, the bands of significant field in the periphery of the NE average magnetograms (Figure 10) were unexpected.
3. The distribution of background field must also be matched between populations in a manner analogous to matching the distributions of location and time (epoch within a solar cycle). That is, there is in fact a bias in the data sets used here, since the NE regions are overall quieter, with less background field, than the PEs (see Figure 11). Rather than just select for “no field above a certain threshold” for the NE regions, areas should be selected which match the pre-emergence background field distribution characteristics of the PEs. This task is not trivial.
4. Related, the spatial distribution of the field may be important, since the seismology signatures are derived from Doppler signals both at the focal point and in an annulus, whose size relates to the depth sampled. Regions emerging into an existing plage area will have a different surrounding flux distribution than very quiet non-emergence areas. Contrariwise, if stable plage areas are chosen preferentially as the NE targets, then a bias is clearly introduced.
5. Utilize helioseismic data and magnetic data from the same source, if at all possible. It was unfortunate that magnetic field data were not readily available for this study from the GONG system. HMI is the logical data source for any follow-on statistical study to what is presented here.
6. Examine 48 hr or more prior to emergence rather than only 24 hr (and, of course, match this for the control data). This will decrease the number of regions available within suitable observing angles, however, will allow additional evolution to be detected.
7. For studies that employ statistical analysis, initial target sample sizes should be 5–10 times larger than assumed sufficient for the final analysis. The robustness of results depends on noise in the data and the many sources of bias. But it also involves an interplay between sample sizes versus the number of variables tested. The larger the sample size, and the larger that size is relative to the number of variables under consideration, the smaller the chance of statistical flukes in outcome. The initial “PE” target list for this study numbered almost 500 regions; after removing targets due to data problems, significant spatial/temporal overlap, matching for latitude/longitude/epoch, and accounting for duty-cycle limitations, each time interval used had $\approx 85\text{--}90$ samples.

5.2. Data Availability

Despite the shortcomings identified above, the present study provides a rich data set for investigating questions of pre-emergence signatures of solar active regions, the sensitivity of results to methodology, etc.

To that end, we make the data sets used in this study available through <http://www.cora.nwra.com/LWSPredictEmergence/>

[Site/Data_Sets.html](#) (following the link that cites this paper). They have been prepared for double-blind tests, in that the data from both PE and NE samples are available but have been randomized with all identifying information removed from filenames and file headers. Also included at that Web site will be an uploadable form by which to submit “answers” to the same Discriminant Analysis code used in Barnes et al. (2012), so that groups interested in direct method comparisons can quantitatively compare performance against our published results.

The authors acknowledge support from NASA contract NNN07CD25C and the hospitality and support of the National Solar Observatory, and also thank the referee for careful reading and comments. This work utilizes data obtained by the Global Oscillation Network Group (GONG) program, managed by the National Solar Observatory, which is operated by the Association of Universities for Research in Astronomy (AURA), Inc. under a cooperative agreement with the National Science Foundation. The data were acquired by instruments operated by the Big Bear Solar Observatory, High Altitude Observatory, Learmonth Solar Observatory, Udaipur Solar Observatory, Instituto de Astrofísica de Canarias, and Cerro Tololo Inter-American Observatory. MDI data were provided by the *SOHO*/MDI consortium. *SOHO* is a project of international cooperation between ESA and NASA. A.C.B. acknowledges collaborative work within the framework of the DFG CRC 963 “Astrophysical Flow Instabilities and Turbulence.”

REFERENCES

- Baldner, C. S., & Schou, J. 2012, [ApJL](#), **760**, 1
- Barnes, G., Birch, A. C., Leka, K. D., & Braun, D. C. 2012, [ApJ](#), submitted
- Bernasconi, P. N., Rust, D. M., Georgoulis, M. K., & Labonte, B. J. 2002, [SoPh](#), **209**, 119
- Birch, A. C., Braun, D. C., & Fan, Y. 2010, [ApJL](#), **723**, 190
- Birch, A. C., Braun, D. C., Leka, K. D., Barnes, G., & Javornik, B. 2012, [ApJ](#), **762**, 132
- Bogdan, T. J. 1986, [SoPh](#), **103**, 311
- Brandenburg, A. 2005, [ApJ](#), **625**, 539
- Braun, D. C. 2012, [Sci](#), **336**, 296
- Braun, D. C., & Birch, A. C. 2008, [ApJL](#), **689**, 161
- Braun, D. C., Birch, A. C., Benson, D., Stein, R. F., & Nordlund, Å. 2007, [ApJ](#), **669**, 1395
- Chaplin, W. J., Elsworth, Y., Miller, B. A., Verner, G. A., & New, R. 2007, [ApJ](#), **659**, 1749
- Christensen-Dalsgaard, J. 2002, [RvMP](#), **74**, 1073
- Corbard, T., Toner, C., Hill, F., et al. 2003, in GONG+ 2002. Local and Global Helioseismology: the Present and Future, ed. H. Sawaya-Lacoste (ESA Special Publication, Vol. 517; Noordwijk: ESA), 255
- Fan, Y. 2009, [LRSP](#), **6**, 4
- Gaiauskas, V., Harvey, K. L., & Proulx, M. 1994, [ApJ](#), **422**, 883
- Giles, P. M. 2000, PhD thesis, Stanford Univ.
- Gizon, L., & Birch, A. C. 2005, [LRSP](#), **2**, 6
- Gizon, L., Birch, A. C., & Spruit, H. C. 2010, [ARA&A](#), **48**, 289
- Hagenaar, H. J., Schrijver, C. J., & Title, A. M. 2003, [ApJ](#), **584**, 1107
- Harvey, J., Tucker, R., & Britanik, L. 1998, in Structure and Dynamics of the Interior of the Sun and Sun-like Stars, ed. S. Korzennik (ESA Special Publication, Vol. 418; Noordwijk: ESA), 209
- Harvey, K. L., & Zwaan, C. 1993, [SoPh](#), **148**, 85
- Hill, F., Bolding, J., Toner, C., et al. 2003, in GONG+ 2002. Local and Global Helioseismology: the Present and Future, ed. H. Sawaya-Lacoste (ESA Special Publication, Vol. 517; Noordwijk: ESA), 295
- Ilonidis, S., Zhao, J., & Kosovichev, A. 2011, [Sci](#), **333**, 993
- Jensen, J. M., Duval, J. T. L., Jacobsen, B. H., & Christensen-Dalsgaard, J. 2001, [ApJL](#), **553**, 193
- Kendall, M., Stuart, A., & Ord, J. K. 1983, The Advanced Theory of Statistics, Vol. 3 (4th ed.; New York: Macmillan)
- Kirkpatrick, S., Gelatt, C. D., & Vecchi, M. P. 1983, [Sci](#), **220**, 671

- Komm, R., Howe, R., & Hill, F. 2009, *SoPh*, **258**, 13
 Komm, R., Howe, R., & Hill, F. 2011, *SoPh*, **268**, 407
 Komm, R., Morita, S., Howe, R., & Hill, F. 2008, *ApJ*, **672**, 1254
 Kubo, M., Shimizu, T., & Lites, B. W. 2003, *ApJ*, **595**, 465
 Leka, K. D., Canfield, R. C., McClymont, A. N., & van Driel-Gesztelyi, L. 1996, *ApJ*, **462**, 547
 Leka, K. D., van Driel-Gesztelyi, L., Nitta, N., et al. 1994, *SoPh*, **155**, 301
 Lindsey, C., & Braun, D. C. 2000, *SoPh*, **192**, 261
 Martens, P., Attrill, G., Davey, A., et al. 2012, *SoPh*, **275**, 79
 Metropolis, N., Rosenbluth, A., Rosenbluth, M., Teller, A., & Teller, E. 1953, *JChPh*, **21**, 1087
 Pearson, F. 1990, *Map Projections: Theory and Applications* (Boca Raton, FL: CRC Press)
 Petrovay, K., & Abuzeid, B. K. 1991, *SoPh*, **131**, 231
 Pojoga, S., & Cudnik, B. 2002, *SoPh*, **208**, 17
 Press, W. H., Teukolsky, S. A., Vetterling, W. T., & Flannery, B. P. 1992, *Numerical Recipes: The Art of Scientific Computing* (2nd.; New York: Cambridge Univ. Press)
 Rudenko, G. V. 2001, *SoPh*, **198**, 5
 Sakurai, T. 1982, *SoPh*, **76**, 301
 Scherrer, P. H., Bogart, R. S., Bush, R. I., et al. 1995, *SoPh*, **162**, 129
 Silverman, B. W. 1986, *Density Estimation for Statistics and Data Analysis* (London: Chapman and Hall)
 Stein, R. F., Lagerfjärd, A., Nordlund, Å., & Georgobiani, D. 2011, *SoPh*, **268**, 271
 Woodard, M. F., & Noyes, R. W. 1985, *Natur*, **318**, 449
 Zhang, H., & Song, M. 1992, *SoPh*, **138**, 69
 Zhao, J., Nagashima, K., Bogart, R. S., Kosovichev, A. G., & Duvall, J. T. L. 2012, *ApJL*, **749**, 5
 Zharkov, S., & Thompson, M. J. 2008, *SoPh*, **251**, 369
 Zwaan, C. 1985, *SoPh*, **100**, 397